Title

Growth of Lithium Dendrites and Globules through a Solid Block Copolymer Electrolyte as a Function of Current Density

Journal

The Journal of Physical Chemistry C, 122(47)

ISSN
1932-7447

Authors

Maslyn, Jacqueline A
Loo, Whitney S
McEntush, Kyle D
et al.

Publication Date
2018-11-29

DOI
10.1021/acs.jpcc.8b06355

Peer reviewed

Growth of Lithium Dendrites and Globules through a Solid Block Copolymer Electrolyte as a Function of Current Density

Jacqueline A. Maslyn [a, b], Whitney S. Loo [a], Kyle D. McEntush [a], Hee Jeung Oh [a], Katherine J. Harry [b, c], Dilworth Y. Parkinson [d], Nitash P. Balsara [a, b, e, *]

[a] Department of Chemical and Biomolecular Engineering, University of California, Berkeley, California 94720, USA

[b] Materials Sciences Division, Lawrence Berkeley National Laboratory, Berkeley, California, 94720, USA

[c] Department of Materials Science and Engineering, University of California, Berkeley, California 94720, USA

[d] Advanced Light Source, Lawrence Berkeley National Laboratory, Berkeley, California 94720, USA

[e] Energy Technologies Area, Lawrence Berkeley National Laboratory, Berkeley, California 94720, USA

* Corresponding author. E-mail: nbalsara@berkeley.edu, Phone: 1-510-642-8973.

ABSTRACT

The uncontrollable non-planar electrodeposition of lithium is a significant barrier to the widespread adoption of high energy density rechargeable batteries with a lithium metal anode. A promising approach for preventing the growth of lithium dendrites is the use of solid polymer electrolytes with a high shear modulus. Current density is the key variable in the electrodeposition of lithium. The present study is the first attempt at quantifying the effect of current density on the geometry and density of dendrites and other protrusions during electrodeposition through a solid polymer electrolyte. The geometry and density of defects formed on the lithium electrode were determined by X-ray microtomography. The tomograms revealed protrusions on the electrodeposited lithium electrodes that were either globular or dendritic, or void defects. The range of current densities over which stable, planar deposition was observed is quantified. At higher current densities, globular protrusions were observed. At the highest current density, both globular and dendritic protrusions were observed. The areal density of protrusion defects increased sharply with current density, while the overall defect density is a weak function of current density. Our work enables comparisons between the experimentally determined onset of non-planar electrodeposition and prevailing theoretical predictions with no adjustable parameters.

INTRODUCTION

Rechargeable batteries are indispensable in the emerging clean energy landscape; especially relevant will be safe, high energy density batteries necessary for the next generations of electric vehicles.[1,2] Batteries that incorporate a solid lithium anode have drawn interest for their significant improvements over Li-ion gravimetric and volumetric energy density.[3–5] In addition, a lithium metal anode is necessary to enable battery chemistries like Li-sulfur and Li-oxygen, which have theoretical energy densities comparable to that of octane.[6] However, a longstanding challenge in rechargeable lithium metal batteries is a tendency to fail due to the growth of protruding lithium dendrites from the metal anode as the battery is charged.[7–9] A promising approach for preventing the growth of lithium dendrites is through the use of solid polymer electrolytes with a high shear modulus.

Lithium dendrites, and the analogous globules observed in solid polymer electrolytes, are a manifestation of uneven current density at the electrode. It is apparent that the formation of lithium dendrites is affected by current density, yet we know of no systematic studies of the effect of current density on their density and morphology in solid polymer electrolytes. Current density has been shown to affect lithium deposition morphology in organic liquid[10,11] and liquid polymer electrolytes[12–15], as well as solid inorganic electrolytes.[16,17] Liquid electrolytes do not have an appreciable shear modulus to counteract the driving forces for lithium dendrite propagation. Inorganic solid electrolytes exhibit a dendritic growth mechanism dependent along grain boundaries.[18] Many previous studies on this subject are restricted to an idealized geometry to accommodate visualization by optical microscopy with several hundred microns between working and counter electrode.[12–15] Electrodeposition of lithium on lithium with an interelectrode distance on the order of tens of microns is more relevant to rechargeable batteries. In the field of solid polymer electrolytes, there have been few studies wherein lithium dendrite growth has been studied as a function of a single parameter.[19,20] Most studies in the literature report on the development of new electrolytes and demonstrate improved performance at a fixed current density.[20–26]

In this paper, we study the effect of current density on the electrochemical deposition of lithium metal through a solid block copolymer electrolyte. In addition to electrochemical characterization, we use the non-invasive technique of synchrotron X-ray tomography to determine the nature and density of protrusions created by electrodeposition. The electrolyte is a nanostructured polystyrene-*block*-poly(ethylene oxide) (PS-*b*-PEO, or SEO) block copolymer in which lithium bis(trifluoromethanesulfone)imide (LiTFSI) salt is dissolved. This solid electrolyte comprises alternating c.a. 60 nm thick PS-rich and PEO-rich lamellae. LiTFSI selectively partitions to the PEO-rich lamellae.[27] This electrolyte combines two desired properties that are ordinarily mutually exclusive: soft PEO domains solvate and conduct lithium ions, while stiff PS domains lend mechanical rigidity to the solid electrolyte. The effect of mechanical rigidity on lithium deposition was first modeled in pioneering work by Monroe and Newman.[28,29] More recent work by Barai et al. has elucidated the effect of current density and mechanical rigidity on lithium deposition.[30,31] Notably, Barai et al. identified regimes of dendritic and non-dendritic lithium deposition as a function of current density and electrolyte modulus. Our approach allows for an experimental test of this theory with no adjustable parameters.

EXPERIMENTAL SECTION

Anionic synthesis and polymer purification. The polystyrene-*block*-poly(ethylene oxide) (SEO) diblock copolymer was synthesized via sequential high-vacuum living anionic polymerization, using *sec*-butyllithium as the initiator for styrene polymerization and P4 *tert*-butylphosphazene base as the promoter for the polymerization of ethylene oxide.[32–34] Trace impurities encountered before the ethylene oxide extension step resulted in dead polystyrene homopolymer chains. Polymers were precipitated in hexanes and then decanted to remove residual small molecules that originated from the synthesis process. The polymers were then re-dissolved in benzene and precipitated two times in hexanes. Then, polymers were subjected to an additional purification step to remove excess polystyrene homopolymer using cyclohexane, in which PS has limited solubility and PEO is not soluble. First, the polymer was re-dissolved in benzene and precipitated in a mixture of hexanes and cyclohexane. The precipitate was isolated and stirred in cyclohexane at room temperature. Then, the process was repeated until gel permeation chromatography (GPC) measurements indicated polymer with a unimodal size distribution. The relevant properties of the SEO copolymer used in this study are provided in Table 1, where ϕ_{EO} refers to the volume fraction of PEO. GPC was conducted on an Agilent 1260 Infinity Series fitted with Water Styragel HR 3 and 4 columns. The polydispersity index (PDI) was measured as 1.1 using a polystyrene standard. The morphology of the block copolymer is lamellar by volume fraction with an approximate domain spacing of 120 nm.

Table 1. Properties of the polymer used in this study.

Name	M_{PS} [kg/mol]	M_{PEO} [kg/mol]	ϕ_{EO}
SEO(115-172)	115	172	0.59

Methods for electrolyte preparation and electrochemical cell fabrication closely mimic those previously reported by Harry et al. and Schauser et al.[19,35–37] All electrolyte preparation was carried out in an argon glove box with less than 2.5 parts per million (ppm) H_2O and less than 2 ppm O_2. All lithium cell assembly was carried out in an argon glove box with less than 5 ppm H_2O and less than 8 ppm O_2.

Li-SEO-Li symmetric cell assembly for polarization and tomographic imaging. — Lithium metal foil was purchased from FMC Lithium at 99.9% purity. The foil thickness was 150 µm. All sample preparation was performed in a glove box filled with Argon gas. A 1/2 or 7/16-inch diameter metal punch was used to cut a polymer electrolyte disc from the previously cast electrolyte film. Three layers of lithium metal foil were stacked on top of a piece of nickel foil, and then pressed at 130 MPa until flat and shiny inside pouch material with a pneumatic press. The lithium electrodes were made by using a 7/16 or 3/8-inch punch to cut through the three layers of lithium foil and nickel foil backing. The two, 450 μm thick, lithium electrodes were used to sandwich the polymer electrolyte membrane. Two 0.25 mm thick stainless steel shims were placed above and beneath the cell to keep the cell flat. Aluminum current collector tabs were then affixed to the stainless steel shims and the sample was vacuum sealed in polypropylene-lined aluminum pouch material.

Conditioning and polarization. Cells were galvanostatically cycled or polarized in an Associated Environmental Systems SD-402 oven using a Maccor Series 4000 Battery Tester. Cells were allowed to equilibrate at the temperature of interest for at least an hour before a current was imposed. Cells were occasionally paused during conditioning or polarization for practical reasons (e.g., while removing a failed cell). Each cell was subjected to fourteen conditioning cycles at 90 °C. During each cycle, a current density of 0.02 mA cm^{-2} was imposed in one direction for 4 hours, followed by a 45 min rest period, followed by the imposition of a constant current density of 0.02 mA cm^{-2} in the opposite direction, followed by another 45 min rest period. The thickness of lithium transferred between the electrodes in each half cycle at 0.02 mA cm^{-2} was 0.4 μm. Cells were then polarized with various current densities at 90 °C between 0.04 mA cm^{-2} and 0.64 mA cm^{-2} until a sudden drop in the voltage required to maintain the target current density was observed. This was taken as the signature of a dendrite short.

Linear rheology measurements. A neat polymer sample disk of diameter 8 mm and thickness 0.6 mm (final thickness after applying normal force) was prepared according to the method described by Schauser et al. [19] Temperatures used for measurements were 120, 110, 100, and 90 °C. Due to limited material, only one sample was made but measurements at 90 and 100 °C, at and near the temperature of interest, were repeated multiple times.

X-ray microtomography. The cells were imaged using hard X-ray microtomography at the Advanced Light Source at Lawrence Berkeley National Laboratory. Monochromatic hard X-rays with energy 22 keV at beamline 8.3.2 at the Advanced Light Source at Lawrence Berkeley National Laboratory illuminated the entire sample, and the X-ray shadow cast by the sample was converted into visible light using a scintillator. An optical microscope magnified this image and converted it into a digital image file. The sample was then rotated by a fraction of a degree and repeatedly imaged until 1,025 images were collected from the sample as it was rotated through 180°. After a series of data processing steps using the software Xi-Cam, these shadow images were converted to cross-sectional slices that were then stacked together to render a 3D reconstruction of the cell. Cells were not removed from their original pouching configuration before being imaged at 2x and/or 5x magnification, corresponding to a pixel size of approximately 3.25 μm or 1.3 μm, respectively. Cross-sectional slices were stacked and rendered by the software ImageJ to be inspected for features of interest. Reconstructed three dimensional (3D) images were analyzed using the commercially available Avizo software package. Data acquisition and analysis builds on methods described by Harry et al. [35]

RESULTS AND DISCUSSION

Each lithium-polymer-lithium cell was first conditioned identically at a low current density as described in the methods section, then galvanostatically polarized at a fixed current density of interest until the cell failed by short circuit. Figure 1a shows typical voltage versus time data obtained during polarization. After one hour of equilibration at 90 °C, a current density, *i*, of 0.32 mA/cm^2 was imposed on this cell. The resulting voltage, shown in Figure 1a, was nearly constant for about 17 hours, after which a precipitous drop in voltage occurred, indicating cell failure by short circuit. Following short circuit failure, the current flow was halted and the cell was imaged. For all cells, charge was passed in only one direction, as shown in Figure 1a. Experiments of this type were repeated at several current densities ranging from 0.04 to 0.64 mA cm^{-2}, and the results are shown in Figure 1b on a plot of C_d versus i. The charge passed before failure, C_d, is calculated using the time of failure and the imposed current density. It is evident that C_d is a sensitive function of i, decreasing monotonically as i is increased from 0.08 to 0.64 mA cm^{-2}. The asterisk in Figure 1b at 0.04 mA cm^{-2} indicates these cells did not fail in spite of galvanostatic polarization for 900 hours. Thus, the reported value of C_d at this current density may be considered as the lower limit.

Figure 2 shows a cross section of a polarized cell acquired using X-ray tomography. This cell was polarized at $i = 0.04$ mA cm^{-2} for 900 h. Under these conditions, a large fraction of the lithium in the top electrode was deposited onto the bottom electrode – the thickness of the deposited lithium layer is calculated to be 175 µm. The measured height of electrodeposited lithium is about 190 µm. The bright band near the top of the cross section in Fig. 2 represents the electrolyte. Also shown in Fig. 2 is the approximate location of the lithium-polymer interface at the initial time, $t = 0$. Only planar lithium electrodeposition was observed in this cell – no protruding features were discernable on the bottom electrode. Thus, we have evidence of a low current density regime where dendrite nucleation and growth is entirely suppressed.

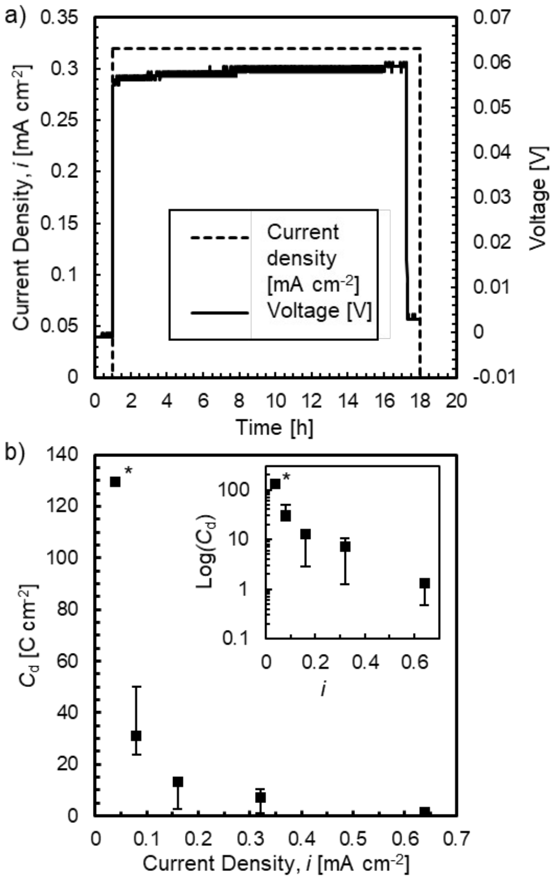

Figure 1. Data obtained from galvanostatically polarized lithium-polymer-lithium symmetric cells. (a) Typical voltage versus time profile. The dashed line gives the applied current density, *i*, and the solid line gives the voltage response, V. The sudden drop in voltage at *t* = 17 h is indicative of a short circuit failure due to the growth of lithium protrusions. (b) The average charge passed per area before failure, C_d, versus applied current density, *i*. C_d decreases dramatically with increasing current density. The asterisk at *i* = 0.04 mA cm^{-2} indicates these cells had not failed at the time point used to calculate C_d, (*t* = 900 h). The inset rescales the y-axis to logarithmic.

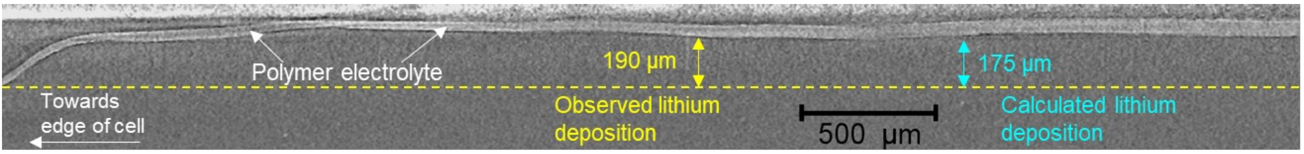

Figure 2. Representative cross section of cell polarized at $i = 0.04$ mA cm^{-2} for $t = 900$ h acquired using X-ray tomography. Lithium was deposited downward through the polymer electrolyte, which appears as a light band extending across the cell near the top of the cross-section. No lithium protrusions were observed. This cell did not short circuit. The yellow arrow shows the thickness of the electrochemically deposited lithium, 190 µm, at a representative location based on the analysis of the tomograms, using the electrolyte's original position at the edge of the cell as a reference point. The blue arrow shows for comparison the estimated thickness of electrochemically deposited lithium, 175 µm, based on the current passed through the cell.

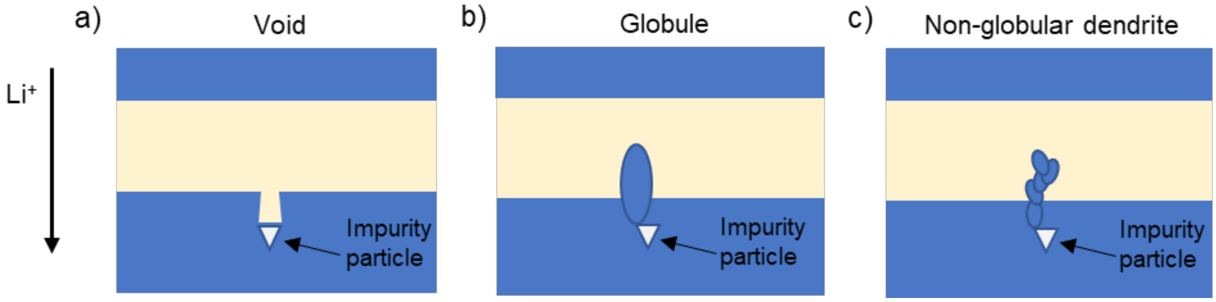

Figure 3. A schematic showing the three types of defects observed in this study: (a) a void defect, (b) a protruding lithium globule, and (c) a protruding non-globular dendrite. In each case, the triangle signifies a crystalline impurity particle, which is observed to be the nucleating site for defective deposition.

The deposition of protruding lithium defects was observed at current densities greater than $i = 0.04$ mA cm^{-2}. The three kinds of defective lithium deposition that we will report in this paper are shown schematically in Fig. 3. All of the defects are nucleated on crystalline impurities. We hypothesize that the impurities are crystals of Li_3N or Li_2O. All of the impurities expected in lithium metal are electronic insulators, and we thus expect them to have similar effects on lithium deposition. In Fig. 3a, we show a void defect, wherein lithium deposition is suppressed in the vicinity of the impurity due to its insulating character. Fig. 3b shows a globular protrusion. This is attributed to local disruption of the solid electrolyte interphase in the vicinity of the impurity. Fig. 3c shows a non-globular, branched structure nucleated at an impurity - this shape most closely resembles the classical dendrite. The depictions in Fig. 3 are based on data we will present shortly, and build on previous studies by Harry et al.[35,36]

Figure 4 shows examples of defective lithium deposition inside failed cells observed by X-ray tomography. In Fig. 4a, X-ray tomography results obtained at $i = 0.08$ mA cm^{-2} are shown. This cell failed at $C_d = 50.1$ C cm^{-2}, corresponding to 68 microns of lithium deposition. Most of the defects at this current density are voids, and lithium deposition is planar. Fig. 4b shows X-ray tomography results obtained at $i = 0.32$ mA cm^{-2}. This cell failed at $C_d = 18.7$ C cm^{-2}, corresponding to 25 microns of lithium deposition. Here we see the formation of a globular defect. At intermediate current densities such as $i = 0.32$ mA cm^{-2}, we observe both voids and globular defects. In Fig. 4c, X-ray tomography results obtained at $i = 0.64$ mA cm^{-2} are shown. This cell failed at $C_d = 0.92$ C cm^{-2}, corresponding to 1.2 microns of lithium deposition. Here, we see the formation of a non-globular dendrite. The protrusion shown exhibits branching and a small tip radius. At this current density, we observe voids, globular defects, and non-globular dendrites. Despite the relatively large current density, all protrusions were observed to nucleate at an impurity particle. Figures 3 and 4 are parallel to each other: Figure 4 shows data corresponding to the idealized schematics in Figure 3.

We observed two classes of failures in short-circuited cells. We refer to the first class as defect-driven failure: an example is shown in Fig. 5a, where we show X-ray tomography results of a cell polarized at $i = 0.32$ mA cm^{-2}. In this class, we observe an electrolyte-spanning protrusion nucleated on an impurity particle. We refer to the second class as fabrication-related failure: an example is shown in Fig. 5b, where we show results from a cell polarized at $i = 0.08$ mA cm^{-2}. In this class, the cell contains no protrusion defects (either globular or non-globular). Instead, we see a break in the electrolyte layer and a concomitant merging of the top and bottom electrodes. It is reasonable to expect that the electrolyte thickness in our cells is not perfectly uniform. We posit that the cell failure mode shown in Fig. 5b occurs due to a local thin spot in the electrolyte membrane. The impurity particles in Fig. 5b result in the formation of void defects, which do not adversely affect cell lifetime. Note that the length scale of the two kinds of failures is very different: protrusions are tens of microns wide, while fabrication-related failures extend across hundreds of microns.

At $i = 0.08$ mA cm^{-2}, we observed two populations of cells with very different lifetimes. Cells that contained signatures of defect-driven failure (i.e., a globular defect nucleated on an impurity particle) exhibited an average lifetime of 10 hours. In contrast, cells that contained signatures of fabrication-related failure exhibited an average lifetime of 181 hours. The deleterious effect of dendrite growth on cell lifetime is clear. At $i \geq 0.16$ mA cm^{-2}, all cells exhibited defect-driven failure.

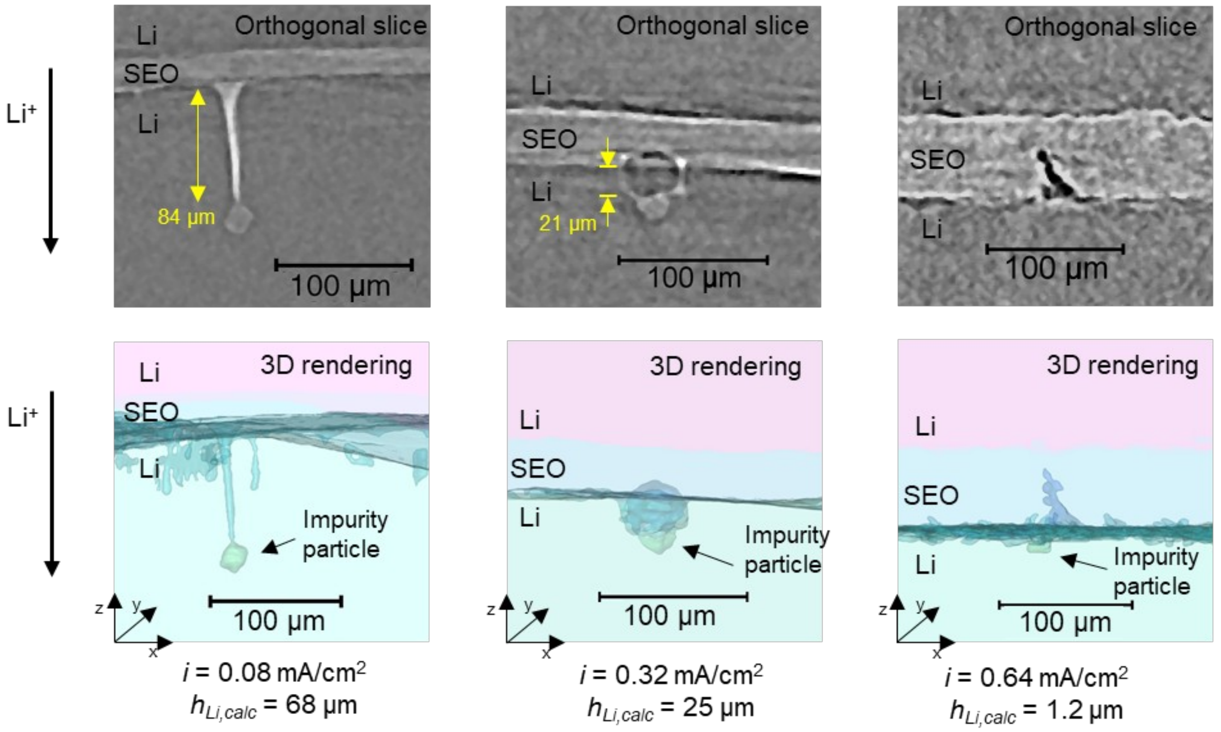

Figure 4. Examples of defective lithium deposition observed in this study by X-ray tomography. The top row shows an orthogonal cross-section through the defect. The bottom row shows a 3D rendered volume that includes the defect. In the 3D rendering, the lower interface between electrolyte and lithium is highlighted. The impurity particle, present in each tomogram, is colored green. Lithium is deposited from top to bottom. The current densities used to polarize the cells are indicated, along with the calculated average thickness of lithium, $h_{Li,calc}$, deposited on the bottom electrode. The yellow arrows are used to estimate the actual thickness of lithium deposited, using the impurity particle as a reference point. In the third cell, not enough lithium was deposited to label the figure. (a) a void defect, (b) a protruding lithium globule, and (c) a protruding non-globular dendrite.

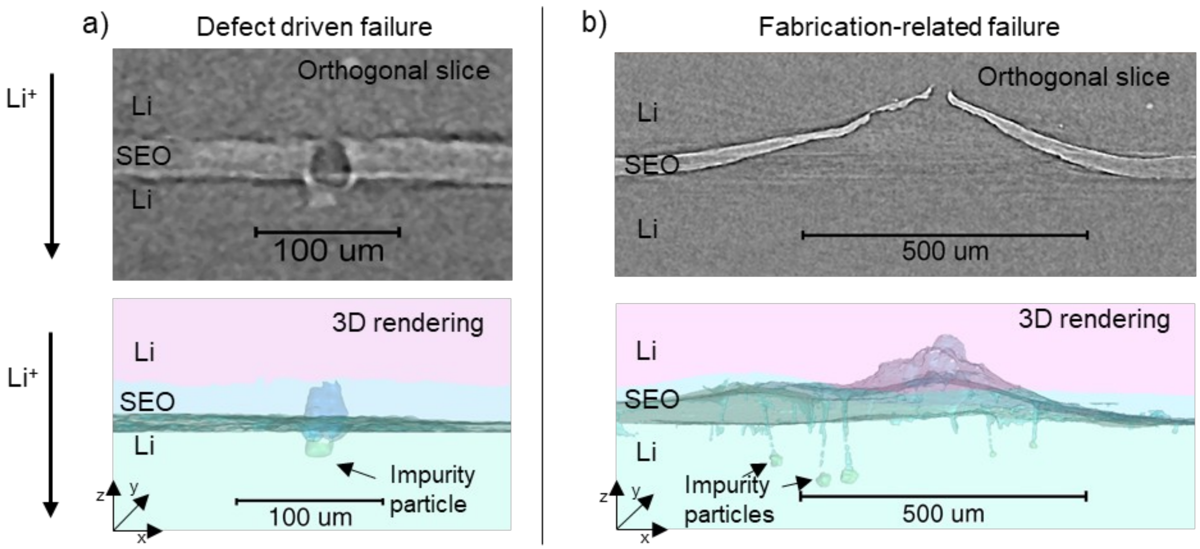

Figure 5. Comparison of defect-driven and fabrication-related modes of cell failure. The top row shows an orthogonal cross-section through the defect. The bottom row shows a 3D rendered volume that includes the defect. In the 3D rendering, the lower interface between electrolyte and lithium is highlighted. (a) A cell polarized at *i* = 0.32 mA cm^{-2} was short-circuited at *t* = 0.7 h and an average of 1.1 µm of lithium plated due to the formation of a lithium globule. (b) A cell polarized at *i* = 0.08 mA cm^{-2} was short-circuited at *t* = 174 h and an average of 68 µm of lithium plated when lithium deposited preferentially through a local thin spot in the polymer electrolyte.

Table 2. Cell lifetime and defect density in failed cells as a function of current density.

Current Density, i ***[mA cm^{-2}]***	***Average C_d*** ***[C cm^{-2}]***	***Average void density,*** ***V [mm^{-2}]***	***Average protrusion density,*** ***P [mm^{-2}]***	***Average defect density, (V + P) [mm^{-2}]***
0.04	129.6*		0	
0.08	31.2	2.2	0.11	2.3
0.16	13.05	1.3	0.77	2.1
0.32	7.18	1.8	1.0	2.8
0.64	1.29	1.4	2.1	3.5

*These cells did not fail in spite of galvanostatic polarization for 900 hours. Thus, the reported value of C_d at this current density may be considered as the lower limit.

The morphology and density of defects are correlated to current density. After imaging a failed symmetric cell by X-ray tomography, the number of defects per unit area counted manually. At each current density, we examined 3 independent cells except at i=0.64 m/cm2 where we examined 2 cells. In each cell an area of 8.7 mm^2 was examined, which was the entire field of view at the magnification chosen (5X). Our observation of defects is thus based on 11 independent cells with a total area of 113 mm^2. (We ran a total of XX cells. In spite of our best effort to maintain the same instrument configuration, some of the tomograms were not as clear as others. For quantification of defect types, we thus chose the 11 cells with the clearest tomograms.) In Table 2, we quantify our observations by reporting the areal density of each defect type observed in failed cells as a function of current density. Non-globular dendrites are only observed at the highest current density ($i = 0.64$ mA cm^{-2}). While some of the observed defects at this current density were clearly dendritic, as shown in Figure 4c, others were globular. Below this current density, all of the protruding defects observed were globular. We use the symbol P to quantify the areal density of protruding defects, both globular and non-globular. We use the symbol V to quantify the areal density of void defects. The dependence of P and V on i is presented in

Table 2. Generally, void density decreases slightly with increasing current density. (Average void density was not calculated at $i = 0.04$ mA cm^{-2} because the cells did not fail.) In contrast, protrusion density increases significantly with increasing current density. Since both void and protrusion defects are nucleated at impurities, one might expect this sum to be related to the number density of impurity particles in the lithium electrode. This is consistent with our observation that ($V + P$) is weakly correlated to current density (see Table 2).

In Figure 6a, we show that P is a monotonically increasing function of i. At $i = 0.04$ mA cm^{-2}, $P = 0$, i.e., no globules or non-globular dendrites were observed at this current density. At $i = 0.08$ mA cm^{-2}, we observe two populations of cells: some cells exhibited globular defects, while others did not. The two data points at this current density in Fig. 6a reflect this fact. At higher current densities, all cells exhibited protruding defects. In Figure 6b, we plot the fraction of protruding defects, f_P, defined as

$$\text{Protrusion fraction, } f_P = \frac{P}{V + P} \qquad (1)$$

as a function of i. The data in Fig. 6a and 6b indicate that the probability of nucleating protrusion defects at impurities increases with increasing current density.

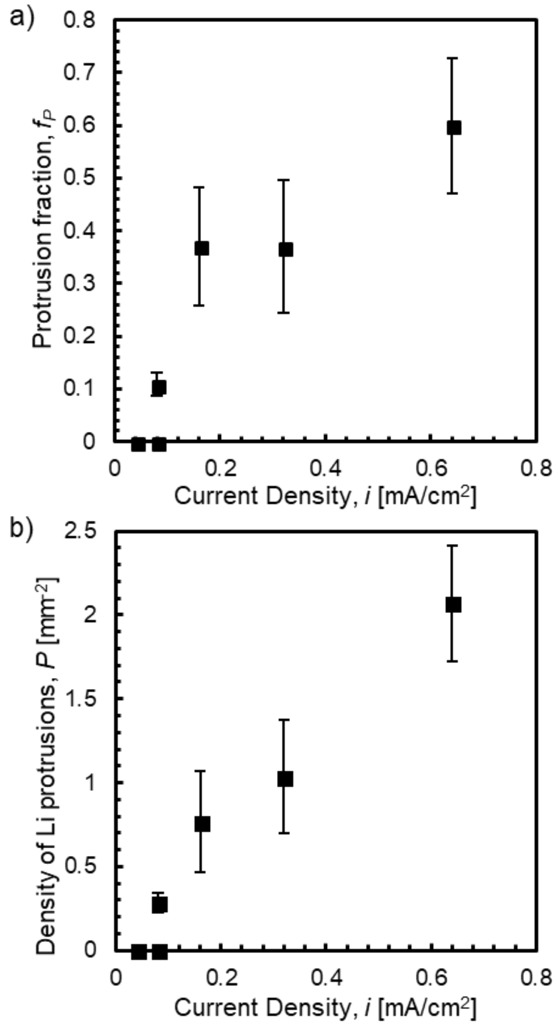

Figure 6. Correlation between current density and defect density in failed cells. (a) The areal density of protruding defects, P, increases with current density. (b) The protrusion fraction, f_P, also increases with current density.

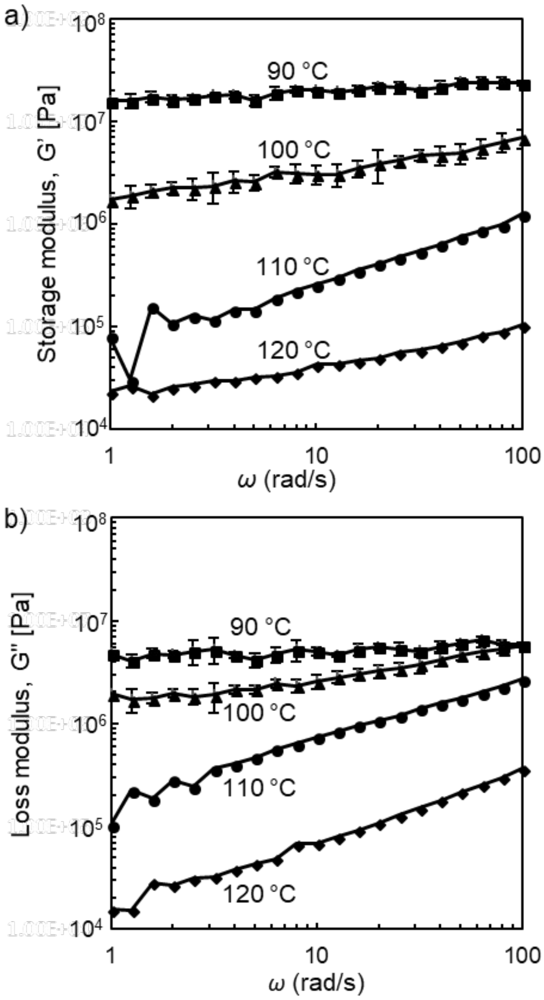

Figure 7. Frequency dependence of shear (a) storage, G’, and (b) loss, G”, moduli measured at 90, 100, 110, and 120 °C. Error bars represent 3 measurements taken and averaged at 100 °C and 90 °C, the temperature of interest.

Fig. 7a and 7b show the measured shear storage (G’) and loss (G”) moduli, respectively, of the polymer used in this study at a range of temperatures from 90 – 120 °C. At 90 °C, the temperature of interest, G’ is nearly independent of frequency (about 2 x 10^7 Pa), and G’ is a factor of 5 larger than G”. These are signatures of an elastic solid. Monroe and Newman first proposed that the parameter that governs lithium dendrite growth is the ratio of the shear moduli of separator and electrode, here the SEO electrolyte and lithium metal, G^{SEO}/G^{Li}. [29] We have used the 3.4 GPa value as G^{Li}, identical to that used by Barai et al. and Monroe and Newman, to calculate this ratio.[29,30] G^{SEO} = 0.02 GPa, the low frequency value of G' at 90 °C. In principle, we should use the shear modulus of a lithium metal protrusion at 90 °C. To our knowledge, the shear modulus of lithium at 90 °C has not yet been reported; however, there is evidence that the shear modulus will have a weak dependence on temperature.[38] It is important to recognize that recent work by Xu et al.[38] and Herbert et al.[39] suggests that the modulus of lithium dendrites may be substantially higher than that of bulk lithium metal and have a strong dependence on crystallographic orientation, a complication that was not included in the work of Monroe and Newman and Barai et al. All of these complications notwithstanding, we compare our results with the simulations of Barai et al., who predicted the stability of lithium deposition as a function of *i* and G^{SEO}/G^{Li}.[30]

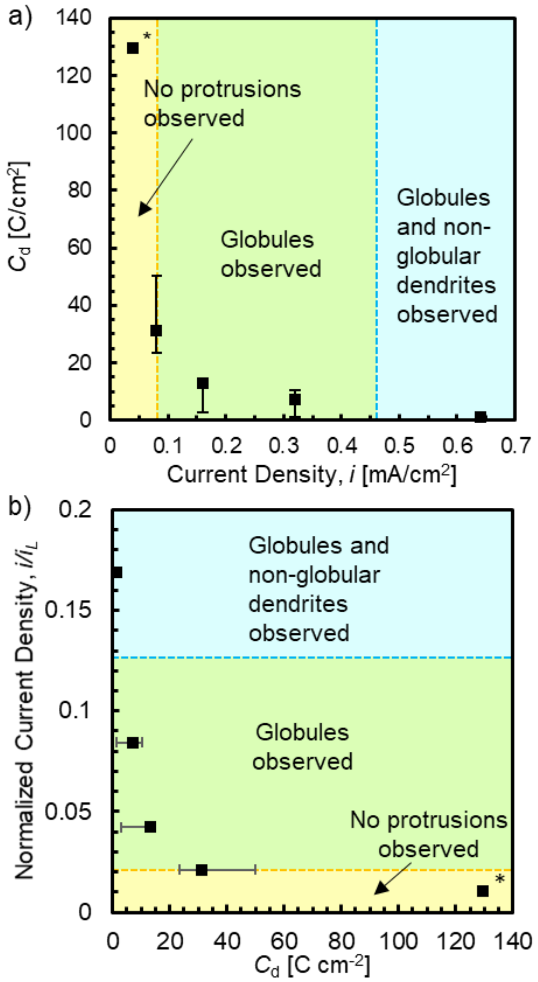

Figure 8. Nature of observed lithium protrusions as a function of current density, *i*, and charge passed before failure, C_d. Observation of no protrusion nucleation at low current densities (yellow area), globules at medium current densities (green area) and non-globular dendrites at high current densities (blue area). The asterisk at $i = 0.04$ mA cm^{-2} indicates these cells had not failed at the time point used to calculate C_d, ($t = 900$ h). (a) C_d as a function of *i*. (b) Normalized current density, i/i_L, as a function of C_d, where i_L is theoretical limiting current (Eq. 2)[28].

Table 3. Parameters used to estimate limiting current.

Parameter	*Value*
c, bulk concentration of salt in the PEO domains of the electrolyte[40]	$1.66\times10^{-3}\left[\frac{mol}{cm^3}\right]$
D, salt diffusion coefficient[40]	$4.5\times10^{-8}[\frac{cm^2}{s}]$
L, electrolyte thickness	$40\times10^{-4}[cm]$
t_{Li}, transference number of the lithium ion[40]	0.05

Fig. 8a describes the effect of current density on the nature of lithium deposition, using Fig. 1b as the basis. At very low current densities, protrusion nucleation and growth is suppressed and no defect-driven failures are observed. At intermediate current densities, partial suppression leads to the observation of lithium globules. At high current densities, globular and non-globular dendrites are observed, along with extremely short cell lifetimes. Fig. 8b recasts C_d as a function of normalized current density, i/i_L. Normalized current density is defined as the current density applied to the cell divided by the theoretical limiting current as defined by Monroe and Newman (Eq. 2).[28] The parameters used to calculate i_L are given in Table 3.

$$i_L=\frac{2\,cDF}{L(1-t_{Li})}\approx3.8\,mA\,cm^{-2} \qquad (2)$$

The qualitative trend demonstrated in Fig. 8 by experiment is consistent with the trend calculated theoretically by Barai et al., who predicted stable lithium deposition at low current densities and unstable lithium deposition at high current densities. The predicted value of i/i_L at the crossover between stable and unstable deposition for $G^{SEO}/G^{Li}\approx0.006$ (we use $G^{Li}\approx3.4$ GPa and $G^{SEO}=0.02$ GPa) is about 0.39. (Using the $G^{Li}\approx9$ GPa value suggested by Xu et al. for (100) Li pillars leads to a crossover $i/i_L\approx$ 0.32 which is not very different from 0.39 determined above.)[38] In contrast, the experimentally determined value of i/i_L at this crossover is about 0.02. The experimentally determined crossover from globular to dendritic protrusions, which occurs at i/i_L of about 0.13, is also significantly lower than theoretical prediction. Three possible reasons for the discrepancy between theory and experiment are: (1) The theoretical model applies to lithium metal anodes devoid of impurities, while our experiments suggest that impurities play an important role. It is conceivable that the current distributions in our experimental cells in the vicinity of the impurities are very different from those in the model. (2) The theoretically predicted limiting current density based on Eq. 2 may be significantly different from the practical limiting current density, due to factors, such as ion transport parameters and block copolymer microstructure, that are highly dependent on salt concentration.[41] (3) The shear modulus of lithium used to make the theoretical calculation, 3.4 GPa, does not take into account geometry and crystallographic orientation, and may not reflect the mechanical properties of the lithium protrusion.

CONCLUSION

The effect of current density on defective lithium deposition in symmetric lithium-polymer-lithium cells was studied by X-ray microtomography. We are particularly interested in the growth of protrusions, which are either globular or dendritic. These defects were nucleated on insulating impurity particles in the lithium electrode. At low current densities ($i = 0.04$ mA cm^{-2}), planar lithium deposition without protrusions is observed. As current density increases ($0.08 \leq i \leq 0.32$ mA cm^{-2}), globular protrusions are obtained. At the highest current density ($i = 0.64$ mA cm^{-2}), globular and dendritic protrusions are obtained. The areal density of protrusions increases monotonically with increasing current density. The lifetime of the symmetric cell correlates with the areal density of protrusions. Our experimental findings were compared to the theoretical predictions of Barai et al.[30], using the measured modulus of the polymer and an estimate for the limiting current density, without resorting to any additional adjustable parameters. The experimentally determined onset of non-planar lithium deposition occurred at a current density about a factor of twenty lower than that predicted by Barai et al. An important limitation of current lithium electrodes is the presence of numerous impurity particles. It is conceivable that the current density range over which planar lithium deposition occurs would increase dramatically is such electrodes were available. We hope that our work will motivate the manufacture of such electrodes in the near future.

AUTHOR INFORMATION

Corresponding Author

*nbalsara@berkeley.edu

Notes

The authors declare no competing financial interest.

ACKNOWLEDGMENTS

This work was supported by the Assistant Secretary for Energy Efficiency and Renewable Energy, Office of Vehicle Technologies of the U.S. Department of Energy under Contract DE-AC02-05CH11231 under the Battery Materials Research Program. Hard X-ray experiments were performed at the Advanced Light Source which is supported by the Director, Office of Science, Office of Basic Energy Sciences, of the U.S. Department of Energy under Contract No. DE-AC02-05CH11231. JAM was supported by a National Science Foundation Graduate Research Fellowship (DGE 2752814).

REFERENCES

(1) Xu, W.; Wang, J.; Ding, F.; Chen, X.; Nasybulin, E.; Zhang, Y.; Zhang, J.-G. Lithium Metal Anodes for Rechargeable Batteries. *Energy Environ. Sci.* **2014**, *7*, 513–537.

(2) Choi, J. W.; Aurbach, D. Promise and Reality of Post-Lithium-Ion Batteries with High Energy Densities. *Nat. Rev. Mater.* **2016**, *1*, 1–16.

(3) Mizushima, K.; Jones, P. C.; Wiseman, P. J.; Goodenough, J. B. Li_xCoO_2 $(0<x\leq 1)$: A New Cathode Material for Batteries of High Energy Density. *Solid State Ionics* **1981**, *3–4*, 171–174.

(4) Tarascon, J.-M.; Armand, M. Issues and Challenges Facing Rechargeable Lithium Batteries. *Nature* **2001**, *414*, 359–367.

(5) Zhang, J.-G.; Wu, X.; Henderson, W. A. *Springer Series in Materials Science: Lithium Metal Anodes and Rechargeable Lithium Metal Batteries*; Springer International Publishing AG Switzerland, 2017.

(6) Balsara, N. P.; Newman, J. Comparing the Energy Content of Batteries, Fuels, and Materials. *J. Chem. Educ.* **2013**, *90*, 446–452.

(7) Takeda, Y.; Yamamoto, O.; Imanishi, N. Lithium Dendrite Formation on a Lithium Metal Anode from Liquid, Polymer and Solid Electrolytes. *Electrochemistry* **2016**, *4*, 210–218.

(8) Lin, D.; Liu, Y.; Cui, Y. Reviving the Lithium Metal Anode for High-Eergy Batteries. *Nat. Nanotechnol.* **2017**, *12*, 194–206.

(9) Aurbach, D.; Zinigrad, E.; Cohen, Y.; Teller, H. A Short Review of Failure Mechanisms of Lithium Metal and Lithiated Graphite Anodes in Liquid Electrolyte Solutions. *Solid State Ionics* **2002**, *148*, 405–416.

(10) Arakawa, M.; Tobishima, S.; Nemoto, Y.; Ichimura, M.; Yamaki, J. Lithium Electrode

Cycleability and Morphology Dependence on Current Density. *J. Power Sources* **1993**, *43–44*, 27–35.

(11) Aurbach, D.; Zinigrad, E.; Teller, H.; Dan, P. Factors Which Limit the Cycle Life of Rechargeable Lithium (Metal) Batteries. *J. Electrochem. Soc.* **2000**, *147*, 1274-1279.

(12) Brissot, C.; Rosso, M.; Chazalviel, J.-N.; Baudry, P.; Lascaud, S. *In Situ* Study of Dendritic Growth in Lithium/PEO-Salt/Lithium Cells. *Electrochim. Acta* **1998**, *43*, 1569–1574.

(13) Brissot, C.; Rosso, M.; Chazalviel, J.-N.; Lascaud, S. *J. In Situ* Concentration Cartography in the Neighborhood of Dendrites Growing in Lithium/Polymer-Electrolyte/Lithium Cells. *Electrochem. Soc.* **1999**, *146*, 4393-4400.

(14) Zhang, X.-W.; Li, Y.; Khan, S. A.; Fedkiw, P. S. Inhibition of Lithium Dendrites by Fumed Silica-Based Composite Electrolytes. *J. Electrochem. Soc.* **2004**, *151*, A1257-A1263.

(15) Liu, S.; Imanishi, N.; Zhang, T.; Hirano, A.; Takeda, Y.; Yamamoto, O.; Yang, J. Lithium Dendrite Formation in Li/Poly(ethylene oxide)-Lithium Bis(trifluoromethanesulfonyl)imide and *N*-Methyl-*N*-propylpiperidinium Bis(trifluoromethanesulfonyl)imide/Li cells. *J. Electrochem. Soc.* **2010**, *157*, A1092-A1098.

(16) Nagao, M.; Hayashi, A.; Tatsumisago, M.; Kanetsuku, T.; Tsuda, T.; Kuwabata, S. *In Situ* SEM Study of a Lithium Deposition and Dissolution Mechanism in a Bulk-Type Solid-State Cell with a Li_2S-P_2S_5 Solid Electrolyte. *Phys. Chem. Chem. Phys.* **2013**, *15*, 18600–18606.

(17) Porz, L.; Swamy, T.; Sheldon, B. W.; Rettenwander, D.; Frömling, T.; Thaman, H. L.; Berendts, S.; Uecker, R.; Carter, W. C.; Chiang, Y. M. Mechanism of Lithium Metal Penetration through Inorganic Solid Electrolytes. *Adv. Energy Mater.* **2017**, *7*, 1–12.

(18) Cheng, E. J.; Sharafi, A.; Sakamoto, J. Intergranular Li Metal Propagation through

Polycrystalline $Li_{6.25}Al_{0.25}La_3Zr_2O_{12}$ Ceramic Electrolyte. *Electrochim. Acta* **2017**, *223*, 85–91.

(19) Schauser, N. S.; Harry, K. J.; Parkinson, D. Y.; Watanabe, H.; Balsara, N. P. Lithium Dendrite Growth in Glassy and Rubbery Nanostructured Block Copolymer Electrolytes. *J. Electrochem. Soc.* **2015**, *162*, 398–405.

(20) Tatsuma, T.; Taguchi, M.; Oyama, N. Inhibition Effect of Covalently Cross-Linked Gel Electrolytes on Lithium Dendrite Formation. *Electrochim. Acta* **2001**, *46*, 1201–1205.

(21) Stone, G. M.; Mullin, S. A.; Teran, A. A.; Hallinan, D. T.; Minor, A. M.; Hexemer, A.; Balsara, N. P. Resolution of the Modulus versus Adhesion Dilemma in Solid Polymer Electrolytes for Rechargeable Lithium Metal Batteries. *J. Electrochem. Soc.* **2012**, *159*, A222-A227.

(22) Ding, F.; Xu, W.; Graff, G. L.; Zhang, J.; Sushko, M. L.; Chen, X.; Shao, Y.; Engelhard, M. H.; Nie, Z.; Xiao, J.; Liu, X.; Sushko, P. V.; Liu, J.; Zhang, J. G. Dendrite-Free Lithium Deposition via Self-Healing Electrostatic Shield Mechanism. *J. Am. Chem. Soc.* **2013**, *135*, 4450–4456.

(23) Bouchet, R.; Maria, S.; Meziane, R.; Aboulaich, A.; Lienafa, L.; Bonnet, J.; Phan, T. N. T.; Bertin, D.; Gigmes, D.; Devaux, D.; Denoyel, R.; Armand, M. Single-Ion BAB Triblock Copolymers as Highly Efficienty Electrolytes for Lithium-Metal Batteries. *Nat. Mater.* **2013**, *12*, 452–457.

(24) Khurana, R.; Schaefer, J. L.; Archer, L. A.; Coates, G. W. Suppression of Lithium Dendrite Growth Using Cross-Linked Polyethylene/Poly(ethylene oxide) Electrolytes: A New Approach for Practical Lithium-Metal Polymer Batteries. *J. Am. Chem. Soc.* **2014**, *136*, 7395–7402.

(25) Villaluenga, I.; Wujcik, K. H.; Tong, W.; Devaux, D.; Wong, D. H. C.; DeSimone, J. M.; Balsara, N. P. Compliant Glass-Polymer Hybrid Single Ion-Conducting Electrolytes for Lithium Batteries. *Proc. Natl. Acad. Sci. U. S. A.* **2015**, *113*, 52–57.

(26) Manuel Stephan, A.; Nahm, K. S. Review on Composite Polymer Electrolytes for Lithium Batteries. *Polymer.* **2006**, *47*, 5952–5964.

(27) Gilbert, J. B.; Luo, M.; Shelton, C. K.; Rubner, M. F.; Cohen, R. E.; Epps III, T. H. Determination of Lithium-Ion Distrituions in Nanostructured Block Polymer Electrolyte Thin Films by X-ray Photoelecttron Spectroscopy Depth Profiling. *ACS Nano* **2015**, *9*, 512–520.

(28) Monroe, C.; Newman, J. Dendrite Growth in Lithium/Polymer Systems. *J. Electrochem. Soc.* **2003**, *150*, A1377-A1384.

(29) Monroe, C.; Newman, J. The Impact of Elastic Deformation on Deposition Kinetics at Lithium/Polymer Interfaces. *J. Electrochem. Soc.* **2005**, *152*, A396-A404.

(30) Barai, P.; Higa, K.; Srinivasan, V. Lithium Dendrite Growth Mechanisms in Polymer Electrolytes and Prevention Strategies. *Phys. Chem. Chem. Phys.* **2017**, *19*, 20493–20505.

(31) Barai, P.; Higa, K.; Srinivasan, V. Effect of Initial State of Lithium on the Propensity for Dendrite Formation: A Theoretical Study. *J. Electrochem. Soc.* **2017**, *164*, 180–189.

(32) Quirk, R. P.; Kim, J.; Kausch, C.; Chun, M. Butyllithium-Initiated Anionic Synthesis of Well-Defined Poly(styrene-*block*-ethylene oxide) Block Copolymers with Potassium Salt Additives. *Polym. Int.* **1996**, *39*, 3–10.

(33) Hadjichristidis, N.; Iatrou, H.; Pispas, S.; Pitsikalis, M. Anionic Polymerization: High Vacuum Techniques. *J. Polym. Sci. Part A: Polym. Chem.* **2000**, *38*, 3211–3234.

(34) Singh, M.; Odusanya, O.; Wilmes, G. M.; Eitouni, H. B.; Gomez, E. D.; Patel, A. J.; Chen, V. L.; Park, M. J.; Fragouli, P.; Iatrou, H. et al. Effect of Molecular Weight on the Mechanical and Electrical Properties of Block Copolymer Electrolytes. *Macromolecules* **2007**, *40*, 4578–4585.

(35) Harry, K. J.; Hallinan, D. T.; Parkinson, D. Y.; Macdowell, A. A.; Balsara, N. P. Detection of

Subsurface Structures Underneath Dendrites Formed on Cycled Lithium Metal Electrodes. *Nat. Mater.* **2013**, *13*, 69–73.

(36) Harry, K. J.; Liao, X.; Parkinson, D. Y.; Minor, A. M.; Balsara, N. P. Electrochemical Deposition and Stripping Behavior of Lithium Metal across a Rigid Block Copolymer Electrolyte Membrane. *J. Electrochem. Soc.* **2015**, *162*, A2699–A2706.

(37) Harry, K. J.; Higa, K.; Srinivasan, V.; Balsara, N. P. Influence of Electrolyte Modulus on the Local Current Density at a Dendrite Tip on a Lithium Metal Electrode. *J. Electrochem. Soc.* **2016**, *163*, 2216–2224.

(38) Xu, C.; Ahmad, Z.; Aryanfar, A.; Viswanathan, V.; Greer, J. R. Enhanced Strength and Temperature Dependence of Mechanical Properties of Li at Small Scales and Its Implications for Li Metal Anodes. *Proc. Natl. Acad. Sci. U. S. A.* **2017**, *114*, 57–61.

(39) Herbert, E. G.; Hackney, S. A.; Dudney, N. J.; Thole, V.; Phani, P. S. Nanoindentation of High-Purity Vapor Deposited Lithium Films: A Mechanistic Rationalization of the Transition from Diffusion to Dislocation-Mediated Flow. *J. Mater. Res.* **2018**, *33*, 1346–1359.

(40) Villaluenga, I.; Pesko, D. M.; Timachova, K.; Feng, Z.; Newman, J.; Srinivasan, V.; Balsara, N. P. Negative Stefan-Maxwell Diffusion Conefficients and Complete Electrochemical Transport Characterization of Homopolymer and Block Copolymer Electrolytes. **2018**, *165*, 2766–2773.

(41) Pesko, D. M.; Timachova, K.; Bhattacharya, R.; Smith, M. C.; Villaluenga, I.; Newman, J.; Balsara, N. P. Negative Transference Numbers in Poly(ethylene oxide)-Based Electrolytes. *J. Electrochem. Soc.* **2017**, *164*, E3569–E3575.

TOC graphic

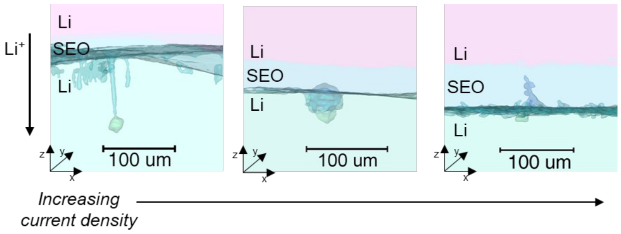
Li⁺
Li
SEO
Li
100 um
z
y
x
Li
SEO
Li
100 um
Li
SEO
Li
100 um
Increasing current density